Redox-Dependent Spatially Resolved Electrochemistry at Graphene and Graphite Step Edges

Aleix G. Güell,*,† Anatolii S. Cuharuc,† Yang-Rae Kim,† Guohui Zhang, Sze-yin Tan, Neil Ebejer, and Patrick R. Unwin*

Department of Chemistry, University of Warwick, Coventry CV4 7AL, United Kingdom. †These authors contributed equally.

ABSTRACT The electrochemical (EC) behavior of mechanically exfoliated graphene and highly oriented pyrolytic graphite (HOPG) is studied at high spatial resolution in aqueous solutions using $Ru(NH_3)_6^{3+/2+}$ as a redox probe whose standard potential sits close to the intrinsic Fermi level of graphene and graphite. When scanning electrochemical cell microscopy (SECCM) data are coupled with that from complementary techniques (AFM, micro-Raman) applied to the same sample area, different time-dependent EC activity between the basal planes and step edges is revealed. In contrast, other redox couples (ferrocene derivatives) whose potential is further removed from the intrinsic Fermi level of graphene and graphite show uniform and high activity (close to diffusion-control). Macroscopic voltammetric measurements in different environments reveal that the time-dependent behavior after HOPG cleavage, peculiar to $Ru(NH_3)_6^{3+/2+}$, is not associated particularly with any surface contaminants but is reasonably attributed to the spontaneous delamination of the HOPG with time to create partially coupled graphene layers, further supported by conductive AFM measurements. This process has a major impact on the density of states of graphene and graphite edges, particularly at the intrinsic Fermi level to which $Ru(NH_3)_6^{3+/2+}$ is most sensitive. Through the use of an improved voltammetric mode of SECCM, we produce movies of potential-resolved and spatially resolved HOPG activity, revealing how enhanced activity at step edges is a subtle effect for $Ru(NH_3)_6^{3+/2+}$. These latter studies allow us to propose a microscopic model to interpret the EC response of graphene (basal plane and edges) and aged HOPG considering the nontrivial electronic band structure.

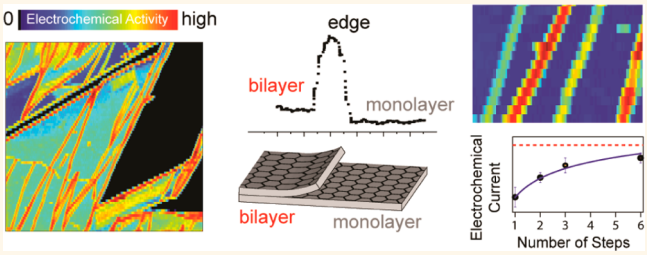

KEYWORDS: graphene · graphite · edges · electrochemistry · electron transfer · HOPG

The significant potential of graphene in next generation electronic,[1] optical,[2] mechanical,[3] and chemical devices[4] is greatly enhanced by the additional possibilities that can be introduced by graphene edges.[5] The strong influence of graphene edges, which can have either armchair (AC) or zigzag (ZZ) termination,[6−8] on the electronic band structure of graphene nanoribbons,[6,9,10] in particular, exemplifies the importance of understanding the physicochemical properties of this structural motif in detail. Previous experimental studies of graphene (and graphite) edges include the use of scanning tunneling microscopy and spectroscopy (STM/STS),[7,11,12] transmission electron microscopy (TEM),[13−17] and micro-Raman spectroscopy.[18,19] These investigations have shown that ZZ and AC graphene edges have distinctly different electronic states and scattering properties as well as unique chemical features.

Graphene is attracting considerable interest in electrochemistry,[20−22] particularly for various energy-related applications.[23−25] Electrochemistry also plays an important role in graphene technology, for example, for edge functionalization,[26−28] which can greatly influence the properties of mesoscopic graphene structures.[23,29] However, despite macroscopic,[30] microscopic,[31] and indirect[26,28] attempts to reveal the electrochemical (EC) behavior of graphene step edges, there are considerable gaps in knowledge particularly pertaining to fundamental microscopic structure−function correlations.

The edge state at graphene or graphite edges, predicted theoretically[6,32] and observed experimentally with STS,[7,10−12] results in an increase of the density of states (DOS) near the intrinsic Fermi level of the uncharged basal plane of graphene. An important question in electrochemistry is

* Address correspondence to p.r.unwin@warwick.ac.uk, a.g.guell@warwick.ac.uk.

Received for review January 25, 2015 and accepted March 10, 2015.

Published online March 10, 2015
10.1021/acsnano.5b00550

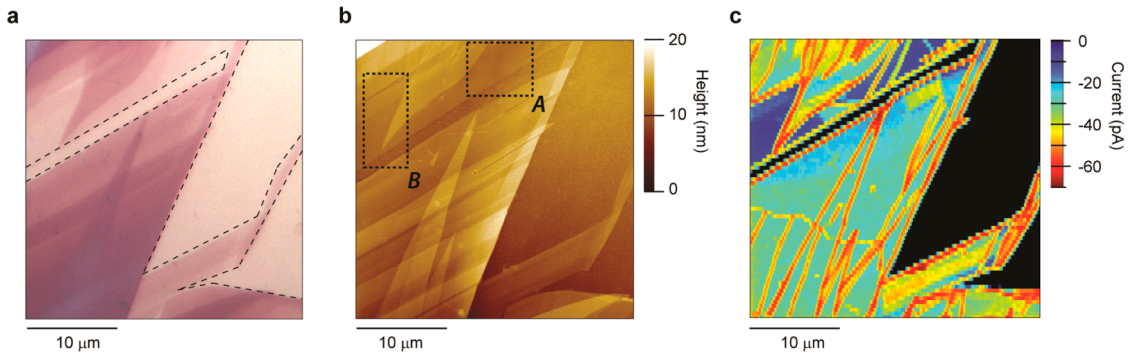

Figure 1. Multimicroscopy of exfoliated graphene (from ZYA grade HOPG) on a Si/SiO_2 substrate. (a) Optical microscopy image (dashed lines define the boundaries between the graphene sample and Si/SiO_2 substrate), (b) AFM topographical image, and (c) SECCM EC map for the reduction of $Ru(NH_3)_6^{3+}$ (5 mM in 25 mM KCl and phosphate buffer, pH = 7.2). The EC map was acquired at a potential $E_{sub} = -0.464$ V ($\eta = -0.198$ V) and 2 μm s^{-1} probe scan rate. For the EC current map, the color scheme was applied only when the EC current value is detectable above 3 times the background current (200 fA); otherwise, it was assigned the black color and coincides with the Si/SiO_2 substrate. In (b), the two areas labeled *A* and *B* exhibiting the lowest EC currents are analyzed in detail in Figure 2.

whether this leads to different electroactivity compared to the neighboring basal surface of graphene (or graphite). For a wide range of reactions, we[33,34] and others[35−37] have shown that the basal surface of freshly cleaved graphite has high intrinsic EC activity that dominates the macroscopic behavior, on typical voltammetric time scales (mass transport rates), such that even if step edges have higher activity it cannot easily be seen against the basal activity[35,36] and is not significant in respect of the overall activity. Here, we demonstrate that on graphene the step state can be detected through the local EC activity of the $Ru(NH_3)_6^{3+/2+}$ couple, whose redox potential lies close to the intrinsic Fermi level of uncharged graphitic materials[38] (for brevity, we will omit "uncharged" later in the text when referring to the intrinsic Fermi level). Indeed, in a recent study, we demonstrated $Ru(NH_3)_6^{3+/2+}$ as a suitable couple to distinguish between metallic and semiconductor single-walled carbon nanotubes (SWNTs),[39,40] as the band gap of semiconducting SWNTs coincided with the $Ru(NH_3)_6^{3+/2+}$ redox potential. On the other hand, for species whose redox potential is far removed from the intrinsic Fermi level (*e.g.*, ferrocene derivatives), we show that the edge state of graphene cannot be distinguished against the high activity of the basal surface.

In this report, we make considerable use of scanning electrochemical cell microscopy (SECCM)[41] to image both exfoliated graphene and highly oriented pyrolytic graphite (HOPG) at high spatial and potential resolution. The ability to build up high-resolution maps of EC activity from thousands of sub-micron-confined measurements, in combination with complementary microscopy techniques, AFM and Raman, provides detailed insights into the EC activity of the main structural motifs—the basal plane and step edges.

RESULTS AND DISCUSSION

High-Resolution Electrochemical Imaging of Graphene. We first consider a large area (30 μm × 30 μm) of exfoliated graphene on Si/SiO_2 (see Methods) comprising regions with single-layer graphene (SLG), bilayer graphene (BLG), and few-layer graphene (FLG), as well as a high density of step edges. This sample allowed the simultaneous assessment of the EC activity of different numbers of graphene layers and step edges within the area interrogated. The sample, located by optical microscopy (Figure 1a) and visualized by AFM (Figure 1b), was imaged by SECCM with a probe end dimension (droplet size) of 400 nm (see Supporting Information (SI), section S1, Figure S1-1). A typical EC map for $Ru(NH_3)_6^{3+}$ reduction at a potential of $E_{sub} = -0.464$ V *vs* Ag/AgCl, 0.1 M KCl, to which all potentials are here onward referred, with cathodic overpotential $\eta = -0.198$ V, is shown in Figure 1c. A significantly lower current is seen at the thinner graphene layers, especially in the graphene zones within the areas marked "*A*" and "*B*" in Figure 1b. Thicker layers, which appear as darker flakes[42,43] in the optical image in Figure 1a, show higher activity as manifested in the higher current magnitude. This behavior is consistent with the reported trend of lower EC activity with lower number of graphene layers.[31,43] Most strikingly, it is evident that the regions of apparently highest activity can be attributed to step edges, although not all step edges exhibit higher EC current compared to the basal surface. Higher EC activity was also found at HOPG step edges with $Ru(NH_3)_6^{3+/2+}$,[36] but the activity difference was much less pronounced. Although different edge chirality gives rise to different electronic states[7,11] and could therefore cause the different EC activity, it is highly unlikely that a constant chirality would be maintained along the entire step lengths,[7,10] which extend up to tens of microns in certain cases (see Figure 1). We analyze the step edge activity in detail below.

The most distinct difference in basal surface activity was seen between SLG and BLG, and to assess in detail the EC activity of these regions, the two areas marked

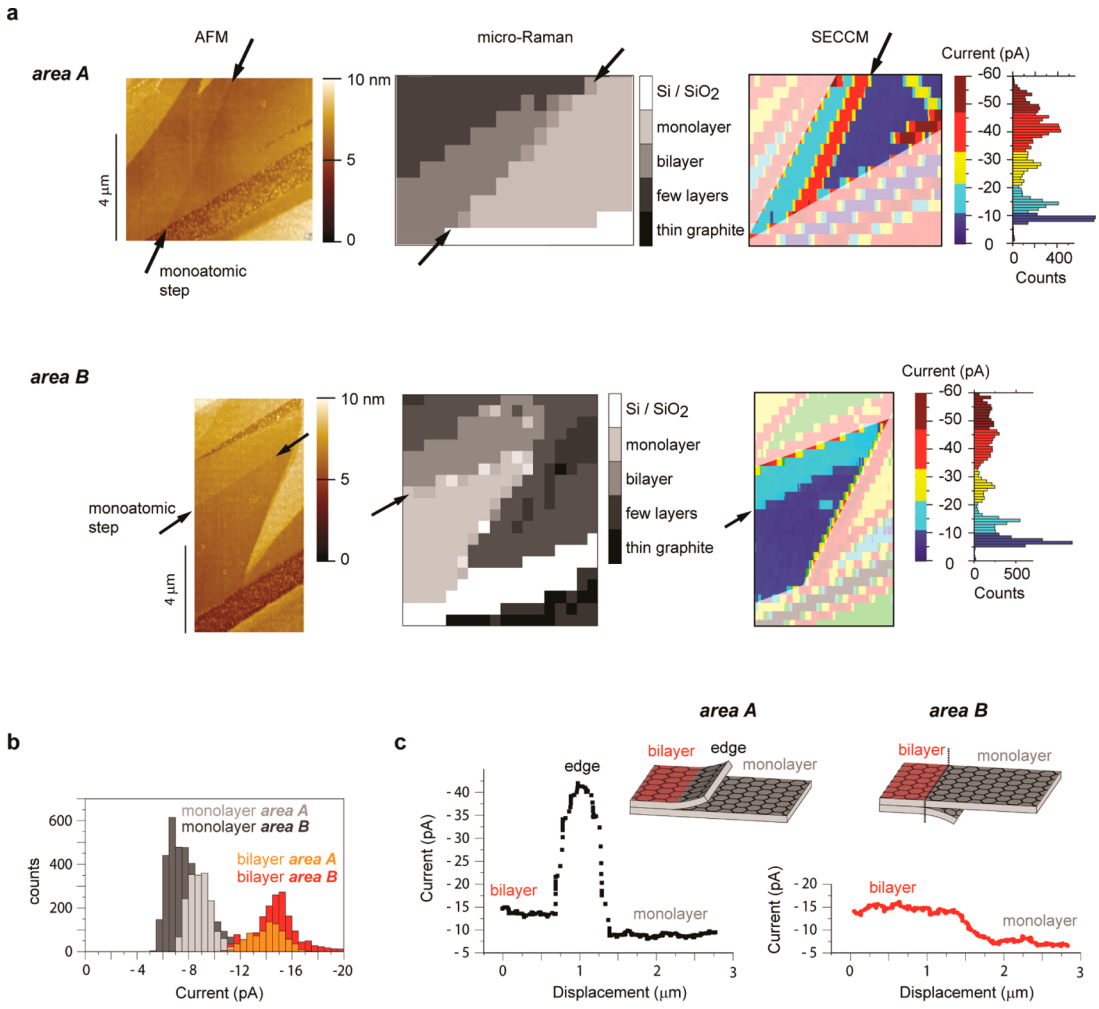

Figure 2. (a) Two areas marked in Figure 1b, labeled *area A* and *area B* studied in detail with three microscopies: AFM (map on the LHS); micro-Raman spectroscopy (map with the number of graphene layers obtained by Raman spectroscopy, details in SI, section S2); SECCM EC map for the reduction of $Ru(NH_3)_6^{3+}$ (5 mM in 25 mM KCl and phosphate buffer, pH = 7.2) acquired at potential $E_{sub} = -0.464$ V ($\eta = -0.198$ V). Histograms of experimental current data are also presented. The black arrows indicate the position of a monatomic step between SLG and BLG in each map. The color scheme for the SECCM EC map has been segmented according to the peaks in the histogram of all data points. (b) EC current data points from the SECCM EC maps for both zoomed areas plotted as histograms. (c) Two SECCM scan profiles on the transition between SLG and BLG in *area A* and *area B* as well as schematics of an exposed and covered step edge.

in Figure 1b were analyzed with micro-Raman spectroscopy.[44] From the spatially resolved Raman spectra, a map of the sample in terms of number of graphene layers (process described in detail in the SI, section S2, Figure S2-3) was obtained and is presented together with AFM topographical maps and SECCM EC maps in Figure 2a. To allow the SLG *versus* BLG areas to be seen easily, only these areas are plotted in true color, while the rest are faded (the unmodified SECCM EC maps are presented in the SI, section S3, Figure S3-1).

In addition to the large volume of data points obtained with SECCM, the technique provides a set of complementary maps obtained simultaneously with EC imaging (see SI, section S3) that were used to confirm the reliability and stability of the meniscus probe during measurements. This is especially relevant for our sample, which possesses large differences in wettability between graphene and Si/SiO_2. These differences may cause the meniscus to be dragged or distorted at boundaries where there is a change in surface chemistry,[45] as exemplified with a slight variation in EC current in Figure 1c, near the ends of the graphene (note the probe scanned from left to right). This is particularly evident from the complementary ion conductance maps presented in SI, section S3, Figure S3-1, for example. Thus, only data within the graphene sample were considered for quantitative analysis.

The EC current measured within a particular graphene facet showed high homogeneity. This is clear from the maps in Figure 2a and the fairly narrow distribution in the EC current histograms in Figure 2b. This behavior is consistent with previous data on sp^2 carbon materials such as graphene,[43,46−49] HOPG,[33,34,50−52] and SWNTs.[39,40,53,54] As evident in Figure 2a, within a particular facet, graphene is a fairly

homogeneously active electrode on the scale of the measurements (defined by the probe size). However, as pointed out above, SLG exhibits substantially less activity with currents of 8 ± 1 pA, (1 standard deviation, SD), compared with BLG currents of 15 ± 1 pA (1 SD) (Figure 2b). Interestingly, while the EC current values for BLG are rather consistent between the two imaged areas (*A* and *B*), as seen in Figure 2b, there is a bigger relative difference between SLG areas. This can be attributed to the strong influence of the substrate on the graphene properties, which is more significant for SLG than for BLG. The presence of oxide and polar impurities on silicon−silicon oxide substrates results in the appearance of electron−hole charge fluctuations (or puddles) on graphene,[55] which influence graphene reactivity.[56] Thus, heterogeneity of the substrate can be transferred to the SLG graphene and is seen in our high-resolution EC measurements. This reasonably explains the differences observed between the two SLG areas. In contrast, in BLG, the fluctuations exist but are much weaker[57] as the top graphene layer is screened by the bottom graphene layer, resulting in more consistent EC current values between the different BLG layers.

The difference in current between SLG and BLG (Figures 1 and 2) and the higher EC current for thicker graphene layers is qualitatively consistent with an increase in the DOS with the number of graphene layers.[58] It is important to point out that with other outer-sphere mediators, whose redox potential was far removed from the intrinsic Fermi level, such as ferrocenylmethyl(trimethylammonium) ($FcTMA^{+/2+}$), a uniform activity was seen, irrespective of the number of graphene layers and with no noticeable enhancement at the step edges, but this is a fast process (close to diffusion-control), making it difficult to resolve kinetics.

A finite element method (FEM) model was developed[59,60] to analyze the measured currents on SLG and BLG (see details in SI, section S5) for $Ru(NH_3)_6^{3+/2+}$, using an effective heterogeneous electron transfer (ET) rate constant, k_{eff}, for a given overpotential/image. This enabled us to avoid suppositions about models of ET kinetics, for reasons that will be explained later. The following boundary condition (eq 1) was considered, in which k_{eff} was the only variable.

$$FD_{Ox}(\partial C_{Ox}/\partial z)_{z=0} = k_{eff}^{(b\ plane)} C_{Ox} \qquad (1)$$

where F is the Faraday constant, C_{Ox} is the near-interface (z = 0) concentration of Ox = $[Ru(NH_3)_6^{3+}]$, which has an effective diffusion coefficient, D_{Ox} = 9.2×10^{-6} cm^2 s^{-1}, incorporating the SECCM electric field effect on mass transport (as determined from the limiting current in this setup).[33,60] Given the relatively high cathodic overpotential (η = −0.198 V), values of $k_{eff}^{(SLG)}$ for SLG of 6.7×10^{-3} cm s^{-1} and $k_{eff}^{(BLG)}$ for BLG of 1.4×10^{-2} cm s^{-1} highlight the relatively slow ET kinetics of this material for $Ru(NH_3)_6^{3+/2+}$ as found in some previous studies.[47,61,62]

Further analysis of areas *A* and *B* reveals a striking difference in EC activity at monatomic steps, with either a very high EC current at a monatomic step edge (marked by arrows on the AFM, micro-Raman, and SECCM images of area *A* of Figure 2a) or an undetectable change in EC current across a step (marked by arrows in area *B* of Figure 2a). Representative SECCM scan profiles of the EC currents across these steps are presented in Figure 2c and clearly highlight this difference in behavior. Ruling out the effect of edge chirality[13,19,63] over long distances (see above), we propose that the step edge showing the enhanced activity is one that is directly in contact or accessible to the solution, while the step edge that does not show enhanced activity compared to the surrounding basal areas (area *B*) is a step covered by a contiguous top graphene screening layer.[64,65] Both types of steps can be reasonably expected from the mechanical exfoliation transfer process. These different configurations are shown schematically in Figure 2c. The curvature at the edges, shown schematically, has been observed on graphite[66] and high-quality graphene nanoribbons.[12] The screening capabilities of graphene also explains why, in Figure 1c, despite a large number of apparent graphene edges, many do not show enhanced activity, suggesting that they are situated beneath monolayer (or multilayer) graphene. We further consider below the origin of the apparent step edge activity seen specifically with $Ru(NH_3)_6^{3+/2+}$ based on enhanced DOS at edges[7,11,12] and the location of the redox potential that is close to that of the intrinsic Fermi level of graphite (and graphene).

Detailed Analysis of Step Edge Activity. By means of the AFM image (details provided in SI, section S2), the EC active step edges were categorized based on the number of monatomic step edges, assigning a value of 335 ± 50 pm height per monolayer step.[67] A schematic map of the EC active steps that were considered is given in Figure 3a, assigning each step into a particular category: overall heights of 1, 2, 3, and 6 monatomic steps. Steps at the boundaries of the graphene sample (with Si/SiO_2) or segments where steps merged were not considered for the analysis and are assigned a gray color in Figure 3a (see SI, section S2, Figure S2-1).

In order to clearly detect the differences in EC current at step edges, the sample was reimaged by SECCM at a lower potential of E_{sub} = −0.364 V, η = −0.098 V (Figure 3b). While the basal plane terraces of graphene show very low EC currents (≈5 pA; see Figure 3b,c), the step edges show much higher current (by up to a factor of 10). A zoom of the area delineated by dashed white lines in Figure 3b is presented in Figure 3c. The intrinsic EC activity of the step edges present in this region was analyzed with nanoscale spatial resolution, by considering SECCM scan

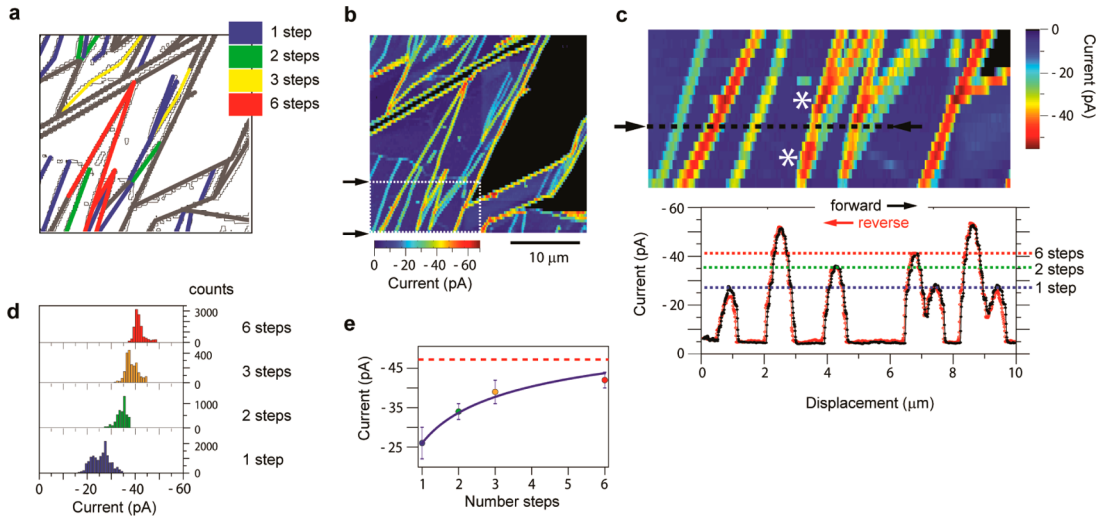

Figure 3. (a) Color map categorization of the number of monatomic step edges (based on AFM data) for enhanced EC active step edges on graphene. Colored in gray are the step edges that were unresolvable precisely by AFM and edges at the graphene−silicon boundary. (b) SECCM EC map for the reduction of $Ru(NH_3)_6^{3+}$ (5 mM in 25 mM KCl and phosphate buffer, pH = 7.2), with the exfoliated graphene sample at a potential $E_{sub} = -0.364$ ($\eta = -0.098$ V). The two black arrows mark a box delineated with a white dashed line which is zoomed in (c). In (c), a forward (black line) and reverse (red line) SECCM EC scan profile of the segment marked with a black dashed line is shown. The peak currents of each step edge accessed were assigned to a color-coded dashed line as in (a). (d) Histograms of the step edge SECCM EC current shown in (b) according to the step edge categorization. Regions where the measured EC current corresponded to the contribution of multiple independent steps (example of merged steps marked with asterisks in the map in (c)) were discarded in the analysis. (e) Plot comparing the experimental EC peak current for step edges and simulated response as a function of the number of monatomic steps making up an edge. The simulation, outlined in the text and in SI, section S5, used $k_{eff}^{(b\ plane)} = 3.4 \times 10^{-3}$ cm s^{-1} and $k_{eff}^{(step)} = 6.8$ cm s^{-1}. The dashed red line shows the simulated EC peak current obtained for the limiting value of a step edge formed by 10 monatomic steps.

profiles.[39,40,53,54] As the redox current is collected continuously at intervals of about 10 nm along each line, EC scan profiles revealed the step edge activity as the SECCM probe moved from the basal surface across the step edge and over the basal surface on the other side of the step. Thus, there is a gradual increase of EC current as the meniscus moves over a step edge, which serves to increase the amount of step edge accessed by the meniscus cell.[39,40,53,54] The peak current value is achieved when the maximum length of step edge is wetted by the meniscus (probe directly over the step), falling in magnitude as the probe moves on. The consistency of values within the same step and between different steps of the same overall height is confirmed by the fairly narrow distribution of the peak current values (Figure 3d) for each type of step, discussed further below, and by the excellent match between forward and reverse scan traces (Figure 3c).

It is clear from the EC scan profile presented in Figure 3c (black dashed scan line marked in the zoomed area in Figure 3c), where seven individual step edges of different height are accessed, that there is a strong effect of step height on peak current. To expand the analysis, EC peak currents were collected and plotted as the histograms in Figure 3d, against the number of monatomic steps making up the overall step feature determined by AFM (steps of 1, 2, 3, and 6 monolayers). This analysis reveals that the EC current increases with the number of step edges (overall step edge height). The FEM model, outlined above and in SI, section S5, was extended to analyze the peak currents, to determine quantitatively how the current scaled with the number of monatomic steps in a particular edge. In this case, we first determined the effective rate constant for the area free from the steps, that is, the basal plane, $k_{eff}^{(b\ plane)}$, yielding $k_{eff}^{(b\ plane)} = 3.4 \times 10^{-3}$ cm s^{-1}. Note that although the driving force for this image was 100 mV less than in Figure 1 and 2, $k_{eff}^{(b\ plane)}$ is on the same order as that for the SLG and BLG measured in Figure 1, consistent with much higher activity of ultrathin graphite compared to SLG and BLG. Then we found the effective rate constant when the probe meniscus was on the steps. Based on the peak current over the edges comprising only monatomic steps, we found $k_{eff}^{(step)} = 7 \pm 3$ cm s^{-1}, and this value was found to predict the current well for all other overall step heights, confirming the trend seen experimentally (Figure 3e). The fact that we see one peak in the EC image and AFM image tells us that steps are closely spaced, but the kinetic analysis tends to suggest that the monatomic steps making up an edge are independent. The computed current for 10 monatomic steps in an edge approached the value of 47 pA (Figure 3e). This is close to the maximum of 50 pA seen experimentally, with the slightly higher experimental values due to exceptional cases such as step edges merging (marked on Figure 3c with an asterisk) or widely spaced multiple steps (distinguishable by

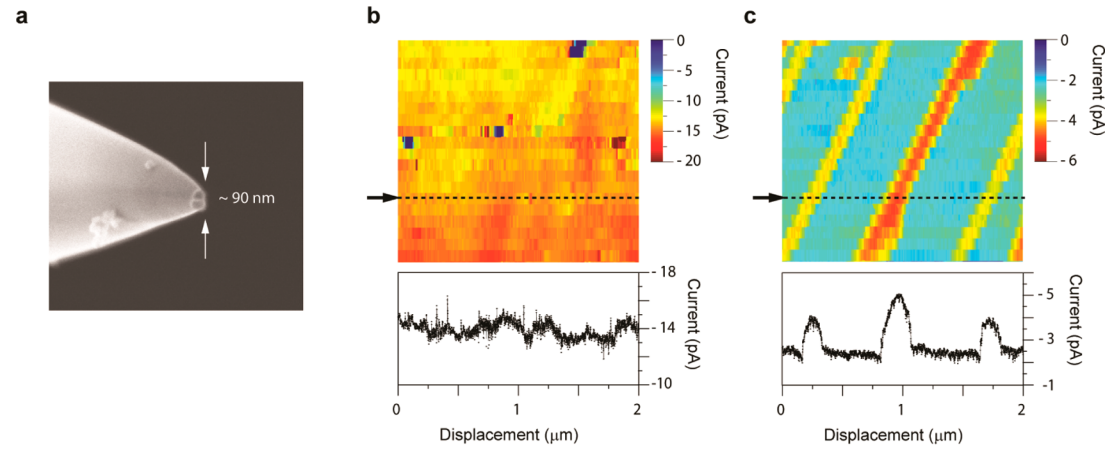

Figure 4. (a) SECCM probe employed for nanoscale SECCM imaging. SECCM EC map for the reduction of $Ru(NH_3)_6^{3+}$ (2 mM in 25 mM KCl and phosphate buffer, pH = 7.2) at ZYA grade HOPG acquired at a driving potential of $E_{sub} = -0.414$ V ($\eta = -0.067$ V) at different times after exfoliation: (b) 10 min (start of scan); (c) 3 h (start of scan). Typical SECCM scan profiles, marked with a black dashed line on the maps, are also shown.

AFM but unresolved by SECCM) (see SI, section S2, Figure S2-1).

Comparison to High-Resolution EC Imaging at HOPG. While step edges on graphene are clearly seen with $Ru(NH_3)_6^{3+/2+}$, previous work employing SECCM on freshly cleaved HOPG samples with the same redox couple did not exhibit this behavior,[33,34] and we seek a rationalization. There are two main differences between the HOPG and graphene samples: (i) the time that elapses between the exfoliation and the EC studies and (ii) the number of graphene layers. The time effect is certainly a factor to consider because, under ambient conditions, contaminants that could accumulate on graphite/graphene surfaces, as well as other issues, may influence on EC response of HOPG.[34,47,68] Note that, for many graphene studies, there is an unavoidable time lapse (of at least a few hours) from the exfoliation of the sample to the final characterization (as an electrode, which requires localization of the graphene on a substrate, establishment of the electrical contacts and the formation of an appropriate EC cell). In contrast, HOPG can be studied as an electrode shortly (within a few seconds for macroscopic studies) after cleavage if the HOPG is already mounted suitably.[34] To investigate the effect of time on the EC response of HOPG, we carried out a set of measurements: (i) as soon as possible after fresh cleavage and (ii) after >3h, being commensurate with the minimum elapsed time for studies of exfoliated graphene. We used both SECCM and also macroscopic electrochemistry in a droplet-cell configuration (see Methods).

To ensure that sufficient step edges were accessed, a ZYA grade HOPG sample was used with a step edge density (between 0.1 and 0.7 μm μm^{-2})[34] slightly higher than that of AM grade HOPG (see Methods for description of HOPG grades). Consequently, to resolve any spatial heterogeneity in EC activity, a sub-100 nm diameter SECCM probe was used (*e.g.*, 90 nm for Figure 4a). Such a resolution, the smallest aerial footprint ever achieved by a factor of >5 for the SECCM technique,[41] is comparable to alternative EC imaging techniques, such as SECM-AFM,[35,36,69,70] but with a much simpler probe preparation and operation, together with the possibility of acquiring a diverse set of complementary maps which are very informative.[39,43,45,54]

Figure 4b,c shows SECCM EC maps for the reduction of $Ru(NH_3)_6^{3+}$ (2 mM) at a driving potential of $E_{sub} = -0.414$ V ($\eta = -0.067$ V) at different times after exfoliation, specifically, 10 min, marking the start of the image (image duration 20 min), and 3 h, respectively. On the 10 min sample (Figure 4b), the EC map is largely featureless, exhibiting a homogeneously active surface (some inactive points, blue, are due to detachment of the nanodroplet during imaging, as confirmed with the ion conductance current complementary map provided in SI, section S3, Figure S3-2a). This result of homogeneous activity is in agreement with previous work at the micro-[33,34] and macroscopic[34,51,52,71,72] scale, at a range of driving forces, including well below the diffusion limit. Interestingly, in light of a recent suggestion that the electroactivity of the HOPG basal plane could be controlled by point defects,[73] the spatial resolution of this probe ($\sim\pi r_{pipet}^2 < 0.01$ μm^2) is particularly powerful as the point defect density on cleaved HOPG, estimated to be in the range of 0.1−10 μm^{-2},[74−78] means that for most positions on the basal surface the pipet would have been located in regions with no point defects, yet the basal plane activity appears uniform and high.

In contrast to Figure 4b, the aged sample (Figure 4c) exhibits an enhanced EC current at the step edges compared to the basal surface. The EC current at the edges attains values between −4 and −5 pA above a background current of −2 pA assigned to terraces. Although the overall EC activity of HOPG has decreased

significantly with time, a direct quantitative comparison of EC current values in Figure 4b,c is difficult due to notable differences in sample wetting by the meniscus, as indicated by the much lower ion conductance current for Figure 4c than for Figure 4b (see SI, section S3, Figure S3-2). Nonetheless, the distinctly higher step edge activity with $Ru(NH_3)_6^{3+/2+}$ on "aged" graphite is at least qualitatively consistent with the observations on graphene.

To assess both the effect of time and possible airborne contaminants on the EC activity, macroscopic measurements were carried out by employing a droplet EC cell configuration[34] (see Methods) on two extreme grades of HOPG in terms of step edge density, AM and SPI-3, with low (0.09%) and high step edge coverage (31%), respectively.[34,51] The simple and fast assembly of this EC cell allowed experiments to be carried out within a few seconds after HOPG exfoliation (if required), with minimal mechanical stress applied to the sample[79] and in a glovebox under N_2, again if required (see Methods). Cyclic voltammograms (CVs) for $Ru(NH_3)_6^{3+}$ reduction were run on AM grade HOPG that was freshly cleaved (droplet placed on the surface in <2−3 s) and on surfaces aged under different environmental conditions for 8 h after exfoliation, that is, in air and in a N_2 atmosphere glovebox. A remarkable difference was observed in the voltammetric response between fresh and aged samples (Figure 5a), changing from an essentially reversible transient (planar diffusion) response on the CV time scale (freshly cleaved surface) to one that was more reminiscent of diffusion to a microelectrode array (with some background current), that is, steady-state diffusion, irrespective of the environmental conditions for aging (see Methods for details). That similar behavior was seen in air and, under a much purer environment, allowed us to reasonably rule out adsorbed contaminants[68] as being responsible for the change in macroscopic voltammetric behavior.

Rather, we propose that the dynamic evolution of the EC activity of HOPG with time is due to a spontaneous delamination of the topmost graphene layers from the remainder of the graphite block. This is a feasible option considering the lamellar structure of HOPG,[65,67] the weak interplanar interaction,[80] and ready structural failures from twisting between layers.[81] We note that delamination could, further, be accentuated by the method of exfoliation or by the EC cell employed, for example, if it introduced additional mechanical stress.[79] Thus, HOPG samples that are aged (or badly cleaved) approach a scenario similar to (multi)layered graphene on top of the remainder of the HOPG block, with some flakes substantially electronically decoupled, leading to a random microelectrode array scenario, consistent with the voltammetric data for aged AM grade HOPG (Figure 5a). Indeed, conductive AFM (C-AFM) experiments carried out on

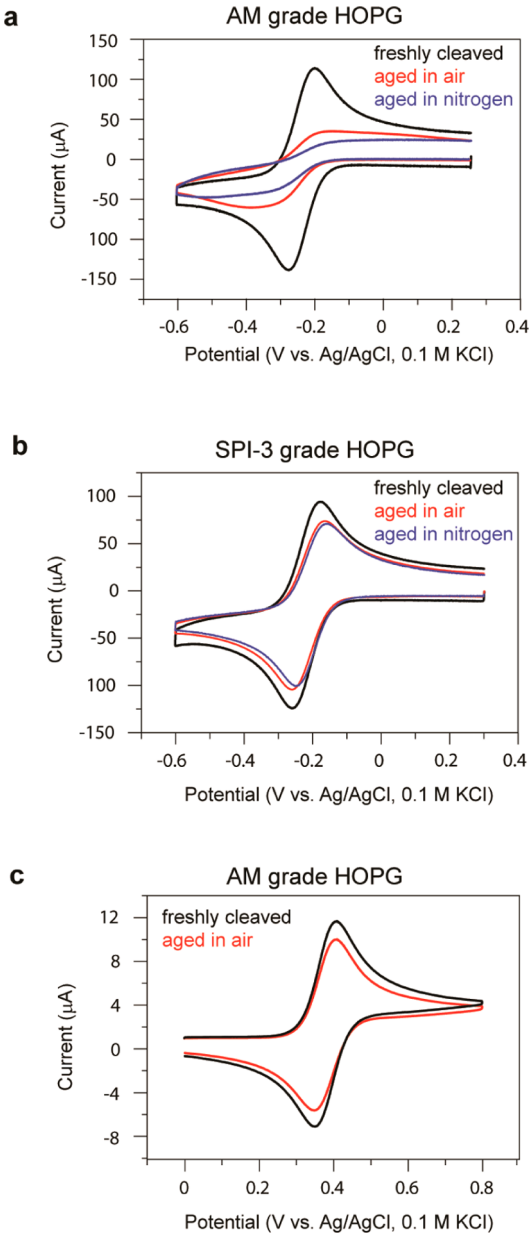

Figure 5. Cyclic voltammograms for the reduction of $Ru(NH_3)_6^{3+}$ (0.25 mM in 0.1 M KCl) at 10 V s^{-1} on HOPG that was either freshly cleaved or aged for 8 h (in air or a nitrogen atmosphere). (a) AM grade HOPG and (b) SPI-3 grade HOPG. (c) Cyclic voltammogram for the oxidation of $FcTMA^+$ (0.25 mM in 1 M KCl) on AM grade HOPG at 0.1 V s^{-1}.

HOPG proved that there was a significant decrease in conductance current within minutes (followed up to 100 min) after exfoliation for both AM and SPI-3 grade HOPG, but with the heterogeneities on a finer scale for SPI-3 HOPG, where the graphite crystallite size is much smaller (see SI, section S2, Figure S2-2).[34]

When macroscopic experiments were carried out on an SPI-3 sample with high step density (Figure 5b), the CVs exhibited reversible behavior, independent of the time elapsed after exfoliation and the environmental conditions (air or inert atmosphere). Since the density of step edges is much higher on SPI-3 HOPG

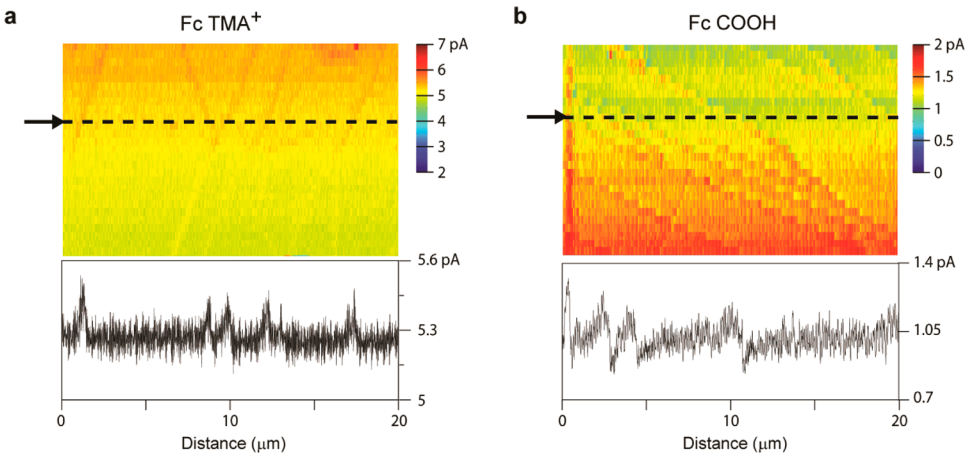

Figure 6. SECCM EC maps on AM grade HOPG and scan profiles (line marked on the map by a dashed line) for the oxidation of (a) FcTMA$^+$ (1 mM in 25 mM KCl and phosphate buffer, pH = 7.2) at a driving potential E_{sub} = 0.236 V (η = −0.010 V), 5 h after exfoliation; (b) ferrocene carboxylic acid (FcCOOH), 0.4 mM in 25 mM KCl and phosphate buffer, pH = 7.2, at a driving potential E_{sub} = 0.136 V (η = 0.002 V), 7 h after exfoliation. The small change in EC current across the image (top part of the map with respect to the bottom part) is due to small drift with time in the ion conductance current (see SI, section S3).

(∼31% coverage compared to the basal surface)[34] and these sites have enhanced activity with $Ru(NH_3)_6^{3+/2+}$ (see above), the macroscopic response thus appears reversible on the time scale of CV measurements.

The total, or partial, detachment of the topmost layer(s) from bulk graphite has important electronic implications, as this detachment leads to a decoupling between the graphene layer(s), with a consequent decrease in the DOS.[58,65] Moreover, the DOS could reasonably become sufficiently low to impact the ET kinetics.[82] The decrease in DOS from graphite to graphene is especially significant at the intrinsic Fermi level.[64,65,83] Because the standard redox potential of the $Ru(NH_3)_6^{3+/2+}$ couple is close to the potential of zero charge (PZC) of graphene (and graphite), where the DOS for (undoped) graphene is theoretically zero (see SI, section S4),[38] the measured kinetics employing this redox mediator are evidently strongly affected by an evolution from the graphite to graphene band structure. On the other hand, the step edge state on graphene[7,11,64] is represented as a peak in the band structure at the intrinsic Fermi level, and as such, this higher DOS would enhance the EC activity at the step edge for the reduction of $Ru(NH_3)_6^{3+}$. Graphite edges also display step edge states,[7,11,84] but the basal plane of graphite has significant DOS at the intrinsic Fermi level (0.0022 states/atom/eV, ref 85), making it more difficult to detect an edge state on the freshly cleaved surface[33,34] (see above). Indeed, the DOS of graphite may be sufficiently high for all outer-sphere redox processes to be in the adiabatic regime,[86,87] such that there would be no difference between the edge and basal surface on freshly cleaved HOPG.

Further outer-sphere redox couples, specifically ferrocene derivatives, were selected for study whose redox potentials were further away from the intrinsic Fermi level.[38] Macroscopic CVs realized on AM grade HOPG (Figure 5c for FcTMA$^+$ oxidation) revealed a reversible response for both a freshly cleaved surface and one aged (8 h in air). This behavior, for a grade of HOPG comprising mainly extended terraces of basal plane, contrasts with that for $Ru(NH_3)_6^{3+/2+}$. This fast reversible behavior for FcTMA$^{+/2+}$ allows us to rule out the possibility that the sluggish kinetics observed in Figure 5a for the reduction of $Ru(NH_3)_6^{3+}$ was a result of macroscopic ohmic drop in the (aged) material.

To back up this analysis, nanoscale EC imaging by SECCM on aged samples (Figure 6a,b) showed homogeneous activity for the oxidation of 2 mM FcTMA$^+$ at E_{sub} = 0.236 V (η = −0.010 V) and 0.4 mM ferrocene carboxylic acid, FcCOOH (pH = 7.2) at E_{sub} = 0.136 V (η = 0.002 V). This is similar to the behavior seen on HOPG discussed above (see Figure 4 and SI, section S3) and is consistent with the idea that, at the energy region of the redox potential of the ferrocene derivatives, graphite and graphene possess a significant DOS, which together with the higher self-exchange ET rate constant for ferrocene derivatives[88] results in a high EC activity of the basal plane. Further support for this proposition comes from the fact that studies of a graphene sample containing monolayer graphene and ultrathin graphite with FcTMA$^{+/2+}$ also showed uniform and comparable activity at a moderate driving potential, below the mass-transport-limited current (see SI, section S3, Figure S3-4).

Dynamic Imaging: SECCM Movies. For a more detailed assessment of the EC behavior at step edges with respect to the basal plane on aged AM grade HOPG samples, the operation of SECCM was modified in order to perform either a linear sweep voltammogram (LSV) or CV (SECCM-LSV or SECCM-CV) at each pixel of the surface map during the scan (see Methods and SI, section S1, for a more detailed description of the

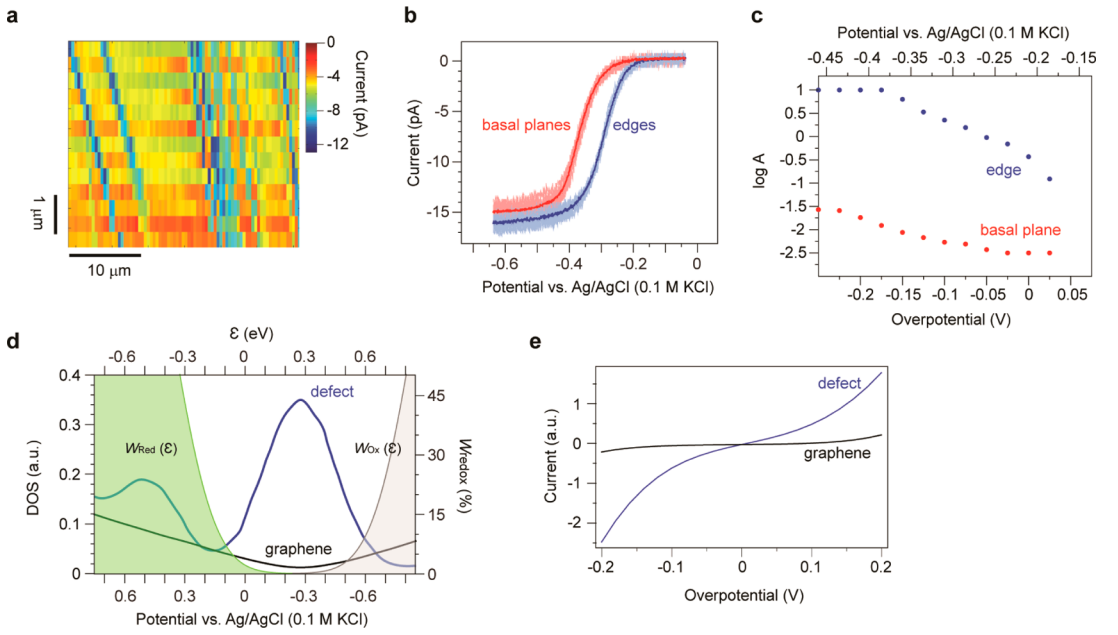

Figure 7. (a) EC map for the reduction of $Ru(NH_3)_6^{3+}$ (in 25 mM KCl and phosphate buffer, pH = 7.2) at AM grade HOPG acquired in SECCM-LSV mode. Each pixel corresponds to the current measured in the corresponding LSV at a potential E_{sub} = −0.32 V (η = −0.11 V). (b) Overlaid are 15 LSVs acquired on step edges (blue) and 20 LSVs on basal plane regions (red). (c) Pre-exponential factors as a function of potential for pure basal plane (red) and edge (blue) extracted from respective SECCM-LSVs shown in (b). (d) Plot of density of states (DOS) of graphene (black) and of defect type V_1(5−9) (blue, data from ref 49) (left axis). Overlaid is the probability density function of redox electrons (right axis): light gray for $W_{Ox}(\varepsilon)$, light green for $W_{Red}(\varepsilon)$. The probability density functions were normalized so that peak height corresponds to 100%. (e) Comparison of kinetic currents at defect sites (blue) and the graphene basal plane (black).

operation). This approach provided an extensive set of potential-resolved SECCM EC maps which could be viewed as movies of EC current *versus* potential sweep [two movies, one for SECCM-LSV imaging with $Ru(NH_3)_6^{3+}$ (200 frames, potential range from E = −0.64 V to E = −0.04 V) and the other for SECCM-CV imaging with $FcTMA^+$ (230 frames, potential range from E = −0.04 V to E = 0.76 V), can be downloaded as a part of the SI, with details in section S1, Table S1]. A representative frame (or SECCM EC map at E_{sub} = −0.32 V, η = −0.11 V) from the movie for the reduction of $Ru(NH_3)_6^{3+}$ is presented in Figure 7a. This snapshot, and the entire movie, is evidently consistent with the earlier images for $Ru(NH_3)_6^{3+}$ reduction on aged HOPG: there is enhanced activity at step edges, with the activity of the basal surface lagging that of the edges until the diffusion limit is reached, where the entire surface becomes essentially uniformly active. In contrast to $Ru(NH_3)_6^{3+}$, we found that for $FcTMA^+$ oxidation there was a totally homogeneous response across the HOPG surface for the entire potential range evaluated (see SI, section S3), as illustrated in the movie.

In Figure 7b, a set of 15 typical LSV curves obtained on step edges and another set of 20 LSV curves on the basal plane are compared. These data were extracted from the SECCM-LSV data file. Clearly, there is a very high level of agreement between the LSVs in each of the two different locations. The LSV on the pure basal plane is shifted cathodically by ≈70 mV (at the half-wave potential) relative to the one with the meniscus located over the basal-and-edge, with potential difference between the 1/4- and 3/4-wave potentials, $E_{3/4} - E_{1/4}$, in both locations in the range of 60−70 mV (close to the reversible limit).

We were able to fit the experimental voltammetric waves for each location in the $Ru(NH_3)_6^{3+/2+}$ movie using a Butler−Volmer formulation with α = 0.5 and $k_0 \approx 0.5$ cm s^{-1} (essentially diffusion-control). However, the formal potentials needed to fit the data were more cathodic than the values obtained from CV measurements at Pt or freshly cleaved HOPG (*cf.* −0.35 V for the pure basal plane wave, −0.28 V for the basal-and-edge wave *vs* −0.21 V at Pt or HOPG), which clearly indicates an inapplicability of the classical model. Please refer to SI, section S5, for further details. We suggest that the observed overpotential of the voltammetric wave on the basal plane, at least in part, is related to the position of the standard (formal) potential of $Ru(NH_3)_6^{3+/2+}$, which is—as highlighted—close to the intrinsic Fermi level of graphene where the DOS is theoretically zero. Likewise, the smaller overpotential on the edge is a consequence of the higher DOS at graphene edges, near the intrinsic Fermi level, than for the basal surface.[49]

On the basis of the established model for voltammetry in SECCM,[60] we performed semiempirical simulations of the characteristic voltammetric waves (Figure 7b, with the details of the simulations given in SI, section S5). To treat the evident overpotential seen in the voltammograms at both the basal surface and edge, we defined and determined a

potential-dependent pre-exponential factor, $A_{basal}(E)$ and $A_{edge}(E)$, that appears in place of k_0 in the Butler–Volmer formulation, setting $\alpha = 0.5$ as expected for an outer-sphere redox couple. We used $E^{0'} = 0.21$ V from the measurements on Pt and HOPG mentioned above. This analysis can be considered as reasonable, as the Butler–Volmer model can be obtained as a limiting case of more complex models of heterogeneous ET. For instance, in the unified expression for the rate constant for adiabatic and nonadiabatic ET in the quantum perturbation theory, the rate constant from the Butler–Volmer model is multiplied by a potential-dependent ratio that originates from a consideration of the electronic states in the electrode and a redox couple,[82] which is somewhat analogous to our approach. In the limiting case of purely adiabatic ET, the ratio becomes a fixed value.

Figure 7c shows how $A_{basal}(E)$ and $A_{edge}(E)$ vary with potential. It can be seen that $A_{basal}(E) \ll A_{edge}(E)$ at all the potentials, as expected, based on the enhanced activity of the edge, and it can further be seen that the transition to the maximum A value occurs at lower potential for the edge site, with A changing more steeply with applied potential for the more active edge, again as expected.

To deepen the analysis of the data in Figures 7b, we turn to the Gerischer framework, which considers the overlap between DOS at an electrode with that of the redox electrons as determining the kinetics of ET,[87,89] with the microscopic kinetic current, i_M, given as

$$i_M = \int_{-\infty}^{+\infty} ek_T(\varepsilon)\rho_M(\varepsilon)\{1 - f(\varepsilon - \varepsilon_F)\}\rho_{redox}(\varepsilon)f(\varepsilon - \varepsilon_{F(redox)})d\varepsilon \quad (2)$$

where k_T is the transmission coefficient, ρ_M is the DOS at the electrode, $f(\varepsilon - \varepsilon_{F(M)})$ is the Fermi function, $\varepsilon_{F(M)}$ is the energy at the Fermi level, ρ_{redox} is the DOS of the redox electrons, $\varepsilon_{F(redox)}$ is the Fermi level of redox electrons, and integration is performed over all the energy levels.

All details of the calculations are relegated to the SI, section S6. To a reasonable approximation, we used the DOS energy profiles from graphene (akin to the basal surface of aged HOPG), defect graphene (as an approximation for the edge state), and $Ru(NH_3)_6^{3+/2+}$ in solution (Figure 7d) to calculate the kinetic currents (no mass transport effects) at the basal and edge sites as a function of applied potential (Figure 7e). For reasons outlined in SI, section S6, we do not seek to calculate absolute current values but rather are interested in the relative difference between the edge and basal sites. It is evident that the relative difference in the DOS potential profile between the edge (defect) and basal graphene, at least in the potential range critical for ET with $Ru(NH_3)_6^{3+/2+}$, results in a much larger current density at the edge than for the basal surface, qualitatively consistent with the experimental data.

Favorable overlap of the electronic states is not the only significant factor in graphene electrochemistry. The chemical (or quantum) capacitance, a measure of the change of the Fermi level relative to the band structure with the amount of charge on the electrode, will also influence ET kinetics. Its relevance has been demonstrated in the evaluation of ET kinetics at single-walled carbon nanotubes.[90,91] Some fraction of the applied electrode potential is spent in shifting the Fermi level relative to the band structure, while the remainder of the potential moves the whole band structure as in a metal electrode. Hence not all of the applied potential will be confined in the compact layer of the electrode, resulting in lower driving force for ET than applied with a potentiostat. Importantly, this will affect the electric double-layer structure in the solution part of the interface with consequences for the kinetics.[82] The relatively high activity of the step edges at graphene and aged HOPG with $Ru(NH_3)_6^{3+/2+}$ effectively creates a nanosized electrode, for which dynamic double-layer effects may be important.[82]

While the analysis provided is valid for the $Ru(NH_3)_6^{3+/2+}$ couple, for other redox systems whose formal potential sits further from the intrinsic Fermi level of graphene (*e.g.*, ferrocene derivatives), the shift of the whole band structure as a consequence of the electric potential and the chemical capacitance has to be considered. The higher DOS of the edge will tend to cause the band structure of the defect to shift along with the Fermi level (similar to a metal), whereas the graphene basal plane band structure will experience a smaller shift due to a more significant chemical capacitance effect (especially around the Dirac point[92]). Therefore, although we do not disregard the possibility that at the potentials for ferrocene derivatives there might also be a difference in EC activity between basal plane and edges, this difference would not be expected to be of the same magnitude as for the $Ru(NH_3)_6^{3+/2+}$ system. In addition, to determine any difference requires techniques with ultrahigh mass transport rates given the high ET kinetics (and self-exchange ET rate constant) of $FcTMA^{+/2+}$ as we noted earlier.

CONCLUSIONS

High-resolution electrochemical microscopy using $Ru(NH_3)_6^{3+/2+}$ as a redox probe, coupled with other techniques in a multimicroscopy approach, revealed complexities in graphite (HOPG) and exfoliated graphene as electrode materials, related to the local electronic and microscopic structure of these materials. We have clearly demonstrated that for $Ru(NH_3)_6^{3+/2+}$ there is strong dependence of the ET kinetics on the number of graphene layers, with monolayer graphene having the slowest rate, increasing for bilayer graphene, and with ultrathin graphite having the fastest kinetics. With the same redox mediator, step edges in

graphene and on HOPG samples that were cleaved and left for a similar time as needed for graphene exfoliation appeared with high contrast in the maps of EC activity (below the diffusion-limited potential). This was in contrast to maps for the oxidation of $FcTMA^+$ and FcCOOH, which produced essentially featureless EC maps, as did $Ru(NH_3)_6^{3+/2+}$ on freshly cleaved HOPG.

We have shown that the capabilities of SECCM can be greatly enhanced by performing potential sweep measurements at each pixel. These measurements establish that the enhanced currents over step edges seen on the maps with fixed (over)potential with $Ru(NH_3)_6^{3+/2+}$ were due to apparent cathodic shifts of the voltammetric wave compared to the reversible case, with the shift being greater at the basal surface of aged graphite than for the step edges. The sensitivity of $Ru(NH_3)_6^{3+/2+}$ to the graphene and graphite structure, in contrast to other redox probes, is because the redox potential of this couple is very close to the intrinsic Fermi level of graphene where the DOS is theoretically zero, whereas the potential of other couples are further removed to values where the DOS of graphene (and graphite) is much higher. Thus, for $Ru(NH_3)_6^{3+/2+}$, the electronic states of the graphene electrode become a limiting factor in the ET rate. This explains the dependency of the observed kinetics for this couple on the number of (graphene) layers and over the enhanced activity of step edges where the local DOS is much higher.

Our experiments have demonstrated plainly a significant time-dependent aspect of the ET kinetics for $Ru(NH_3)_6^{3+/2+}$ on HOPG. There is strong evidence from our measurements (voltammetry and C-AFM) and others (STM/STS) in the literature[65] that spontaneous delamination of the topmost layers of HOPG occurs with time, which leads to a surface made of electronically decoupled regions that are nothing but mono-, few-, and multilayer graphene. In the light of this, it becomes understandable why, for $Ru(NH_3)_6^{3+/2+}$, in particular, aged HOPG produces (a) SECCM images that feature enhanced currents over step edges, as seen for graphene, and (b) macroscopic voltammetry responses that are initially indicative of relatively fast kinetics, but the response evolves rapidly with time due to the microscopic phenomena identified.

METHODS

Sample Preparation. Mechanically exfoliated graphene samples were prepared by the well-known "scotch tape" method from pieces of ZYA grade HOPG (GE Advanced Ceramics, USA) and Natural Kish graphite (Graphene Supermarket, NY, USA) and placed on a Si/SiO_2 substrate (IDB Technologies Ltd.; n-type Si, 525 μm thick with 300 nm of thermally grown SiO_2). In addition to the inertness and flatness of the substrate, the use of Si/SiO_2 as a substrate allowed graphene flakes to be located (and their thickness quantified) by optical microscopy.[42] This enabled the easy establishment of electrical contacts (silver conductive paint, RS components, UK) and further characterization of the areas studied electrochemically by AFM and micro-Raman spectroscopy.

Studies of HOPG utilized either ZYA grade (GE Advanced Ceramics, USA), SPI-3 grade (SPI Supplies, Aztech Trading, UK), or an ungraded but high-quality sample kindly provided by Prof. R.L. McCreery (University of Alberta, Canada), originating from Dr. A. Moore (Union Carbide, now GE Advanced Ceramics) and herein referred to as AM grade HOPG.

Scanning Electrochemical Cell Microscopy. SECCM[41,45,60] experiments are described in detail in the SI, sections S1 and S3. Briefly, the SECCM tip was a double-barreled theta pipet which was sharpened to the desired dimensions (≈400 or 90 nm diameter depending on the experiment) by means of a laser puller (P-2000, Sutter Instrument Co., USA). The pipet, filled with the electrolyte solution of interest and quasi-reference counter electrodes (QRCEs), one inserted into each barrel (see SI, section S1), was approached toward the surface until contact was made with the tiny meniscus at the tapered end, without contact from the probe itself. The probe was then scanned across the surface by means of piezoelectric positioners. Electrochemical measurements were performed in the confined area defined by the meniscus created between the tip and sample. Two different modes of SECCM were employed in the present work: SECCM at a fixed potential and SECCM-CV or SECCM-LSV mode.

SECCM (at fixed potential) measured the EC surface current continuously, while the probe was scanned across the surface at constant tip−sample distance at a predetermined electrode potential.[39,43,54] In this imaging mode, the data acquisition rate was set at 10 μs with 512 measurements averaged per data point. Depending on the scan rate used, a point was acquired every 0.8−10 nm during scanning (see SI, section S1).

For SECCM-CV (or SECCM-LSV in the case of a linear sweep voltammogram), once in meniscus contact with the surface, the probe was scanned across the substrate in a raster-mode at a constant tip−sample distance. A number of pixels per scan area was defined (based on the tip dimensions and sample area), in each of which a CV (or LSV) was performed by sweeping the potential and measuring the corresponding EC current (see SI section S1 and Table S1 for details). Between voltammograms (CV or LSV, carried out at a 200 mV s^{-1}), the probe was moved laterally, maintaining the tip−sample distance constant, to the next position. This mode allowed a set of EC surface current maps at a wide range of potentials, presented in the SI in the form of movies, revealing the evolution of the EC surface current *versus* time (potential). For the data acquisition rate used, EC surface current maps were obtained every ≈4 mV for SECCM-CV and every ≈1 mV for SECCM-LSV (see movies (avi files) in SI).

Macroscopic Electrochemical Experiments. These were carried out in a three-electrode cell formed by placing a 20 μL droplet of solution onto the HOPG sample (working electrode) and inserting a platinum wire and a Ag/AgCl wire acting as the counter electrode and the reference electrode, respectively. The time required for the assembly of the cell and start of the measurements was below 10 s (2−3 s to place the drop of solution after exfoliation). For the experiments in a controlled atmosphere, cleavage of the sample and measurements were performed in a nitrogen-filled glovebox (COY Lab, USA). After the desired elapsed time (8 h), the assembly of the EC cell and measurements were carried out inside the glovebox, where the oxygen level was maintained below 1 ppm. All EC measurements were performed with a CHI 600 electrochemical workstation (CH Instruments, TX, USA).

Sample Characterization. Raman spectroscopy was performed with a micro-Raman (InVia micro-Raman, Renishaw, UK) equipped with a HeNe 633 nm laser and a 100× lens. The assignment of the number of graphene layers was based on the 2D band (2650 cm^{-1}). More details of data processing are provided in the SI, section S2. AFM characterization was carried

out in tapping mode (Enviroscope, Veeco-Bruker). Optical microscopy was employed to locate and evaluate qualitatively the graphene quality. Images of graphene were acquired using a digital camera (Spot, Diagnostic Instruments, USA) attached to a BH2 optical microscope (Olympus, Japan) with a 50×/0.7 NA optical lens (Neo SPlan, Olympus, Japan).

Conflict of Interest: The authors declare no competing financial interest.

Acknowledgment. This work was supported by the European Research Council (ERC-2009-AdG 247143-QUANTIF) and the EPSRC (EP/H023909/1). A.S.C. and G.Z. also acknowledge support by Chancellor's International Scholarships from the University of Warwick. The National Research Foundation of Korea is also acknowledged by Y.-R.K. (2012R1A6A3A03039226). We are indebted to Dr. Kim McKelvey and Dr. Alex Colburn for designing and building instrumentation. Special thanks to Prof. R.L. McCreery for providing the high-quality HOPG sample used in this study. Some equipment used in this research was obtained through Birmingham Science City with support from Advantage West Midlands and the European Regional Development Fund.

Supporting Information Available: Principles of SECCM, AFM images, results of Raman spectroscopy (spectra and maps), complementary SECCM maps, finite element simulations, and calculations of ET rate. This material is available free of charge via the Internet at http://pubs.acs.org.

REFERENCES AND NOTES

1. Schwierz, F. Graphene Transistors. *Nat. Nanotechnol.* **2010**, *5*, 487–496.
2. Koppens, F. H. L.; Mueller, T.; Avouris, P.; Ferrari, A. C.; Vitiello, M. S.; Polini, M. Photodetectors Based on Graphene, Other Two-Dimensional Materials and Hybrid Systems. *Nat. Nanotechnol.* **2014**, *9*, 780–793.
3. Eichler, A.; Moser, J.; Chaste, J.; Zdrojek, M.; Wilson Rae, I.; Bachtold, A. Nonlinear Damping in Mechanical Resonators Made from Carbon Nanotubes and Graphene. *Nat. Nanotechnol.* **2011**, *6*, 339–342.
4. Schedin, F.; Geim, A. K.; Morozov, S. V.; Hill, E. W.; Blake, P.; Katsnelson, M. I.; Novoselov, K. S. Detection of Individual Gas Molecules Adsorbed on Graphene. *Nat. Mater.* **2007**, *6*, 652–655.
5. Jia, X.; Campos-Delgado, J.; Terrones, M.; Meunier, V.; Dresselhaus, M. S. Graphene Edges: A Review of Their Fabrication and Characterization. *Nanoscale* **2011**, *3*, 86–95.
6. Nakada, K.; Fujita, M.; Dresselhaus, G.; Dresselhaus, M. S. Edge State in Graphene Ribbons: Nanometer Size Effect and Edge Shape Dependence. *Phys. Rev. B* **1996**, *54*, 17954–17961.
7. Kobayashi, Y.; Fukui, K.; Enoki, T.; Kusakabe, K.; Kaburagi, Y. Observation of Zigzag and Armchair Edges of Graphite Using Scanning Tunneling Microscopy and Spectroscopy. *Phys. Rev. B* **2005**, *71*, 193406.
8. Girit, Ç. Ö.; Meyer, J. C.; Erni, R.; Rossell, M. D.; Kisielowski, C.; Yang, L.; Park, C.-H.; Crommie, M. F.; Cohen, M. L.; Louie, S. G.; Zettl, A. Graphene at the Edge: Stability and Dynamics. *Science* **2009**, *323*, 1705–1708.
9. Son, Y. W.; Cohen, M. L.; Louie, S. G. Energy Gaps in Graphene Nanoribbons. *Phys. Rev. Lett.* **2006**, *97*, 216803.
10. Ritter, K. A.; Lyding, J. W. The Influence of Edge Structure on the Electronic Properties of Graphene Quantum Dots and Nanoribbons. *Nat. Mater.* **2009**, *8*, 235–242.
11. Niimi, Y.; Matsui, T.; Kambara, H.; Tagami, K.; Tsukada, M.; Fukuyama, H. Scanning Tunneling Microscopy and Spectroscopy of the Electronic Local Density of States of Graphite Surfaces near Monoatomic Step Edges. *Phys. Rev. B* **2006**, *73*, 085421.
12. Tao, C.; Jiao, L.; Yazyev, O. V.; Chen, Y.-C.; Feng, J.; Zhang, X.; Capaz, R. B.; Tour, J. M.; Zettl, A.; Louie, S. G.; et al. Spatially Resolving Edge States of Chiral Graphene Nanoribbons. *Nat. Phys.* **2011**, *7*, 616–620.
13. Schäffel, F.; Wilson, M.; Bachmatiuk, A.; Rümmeli, M. H.; Queitsch, U.; Rellinghaus, B.; Briggs, G. A. D.; Warner, J. H. Atomic Resolution Imaging of the Edges of Catalytically Etched Suspended Few-Layer Graphene. *ACS Nano* **2011**, *5*, 1975–1983.
14. Girit, Ç. Ö.; Meyer, J. C.; Erni, R.; Rossell, M. D.; Kisielowski, C.; Yang, L.; Park, C.-H.; Crommie, M. F.; Cohen, M. L.; Louie, S. G.; et al. Graphene at the Edge: Stability and Dynamics. *Science* **2009**, *323*, 1705–1708.
15. Jia, X.; Hofmann, M.; Meunier, V.; Sumpter, B. G.; Campos-Delgado, J.; Romo-Herrera, J. M.; Son, H.; Hsieh, Y.-P.; Reina, A.; Kong, J.; et al. Controlled Formation of Sharp Zigzag and Armchair Edges in Graphitic Nanoribbons. *Science* **2009**, *323*, 1701–1705.
16. Suenaga, K.; Koshino, M. Atom-by-Atom Spectroscopy at Graphene Edge. *Nature* **2010**, *468*, 1088–1090.
17. Liu, Z.; Suenaga, K.; Harris, P. J. F.; Iijima, S. Open and Closed Edges of Graphene Layers. *Phys. Rev. Lett.* **2009**, *102*, 015501.
18. Cançado, L. G.; Pimenta, M. A.; Neves, B. R. A.; Dantas, M. S. S.; Jorio, A. Influence of the Atomic Structure on the Raman Spectra of Graphite Edges. *Phys. Rev. Lett.* **2004**, *93*, 247401.
19. Casiraghi, C.; Hartschuh, A.; Qian, H.; Piscanec, S.; Georgi, C.; Fasoli, A.; Novoselov, K. S.; Basko, D. M.; Ferrari, A. C. Raman Spectroscopy of Graphene Edges. *Nano Lett.* **2009**, *9*, 1433–1441.
20. Chen, D.; Tang, L.; Li, J. Graphene-Based Materials in Electrochemistry. *Chem. Soc. Rev.* **2010**, *39*, 3157–3180.
21. Brownson, D. A. C.; Kampouris, D. K.; Banks, C. E. Graphene Electrochemistry: Fundamental Concepts through to Prominent Applications. *Chem. Soc. Rev.* **2012**, *41*, 6944–6976.
22. Ambrosi, A.; Chua, C. K.; Bonanni, A.; Pumera, M. Electrochemistry of Graphene and Related Materials. *Chem. Rev.* **2014**, *114*, 7150–7188.
23. Li, Y.; Zhou, W.; Wang, H.; Xie, L.; Liang, Y.; Wei, F.; Idrobo, J.-C.; Pennycook, S. J.; Dai, H. An Oxygen Reduction Electrocatalyst Based on Carbon Nanotube–Graphene Complexes. *Nat. Nanotechnol.* **2012**, *7*, 394–400.
24. Stoller, M. D.; Park, S.; Zhu, Y.; An, J.; Ruoff, R. S. Graphene-Based Ultracapacitors. *Nano Lett.* **2008**, *8*, 3498–3502.
25. Pak, A. J.; Paek, E.; Hwang, G. S. Impact of Graphene Edges on Enhancing the Performance of Electrochemical Double Layer Capacitors. *J. Phys. Chem. C* **2014**, *118*, 21770–21777.
26. Zach, M. P.; Ng, K. H.; Penner, R. M. Molybdenum Nanowires by Electrodeposition. *Science* **2000**, *290*, 2120–2123.
27. Delamar, M.; Hitmi, R.; Pinson, J.; Saveant, J. M. Covalent Modification of Carbon Surfaces by Grafting of Functionalized Aryl Radicals Produced from Electrochemical Reduction of Diazonium Salts. *J. Am. Chem. Soc.* **1992**, *114*, 5883–5884.
28. Sharma, R.; Baik, J. H.; Perera, C. J.; Strano, M. S. Anomalously Large Reactivity of Single Graphene Layers and Edges toward Electron Transfer Chemistries. *Nano Lett.* **2010**, *10*, 398–405.
29. Wagner, P.; Ewels, C. P.; Adjizian, J.-J.; Magaud, L.; Pochet, P.; Roche, S.; Lopez-Bezanilla, A.; Ivanovskaya, V. V.; Yaya, A.; Rayson, M.; et al. Band Gap Engineering *via* Edge-Functionalization of Graphene Nanoribbons. *J. Phys. Chem. C* **2013**, *117*, 26790–26796.
30. Yuan, W.; Zhou, Y.; Li, Y.; Li, C.; Peng, H.; Zhang, J.; Liu, Z.; Dai, L.; Shi, G. The Edge- and Basal-Plane-Specific Electrochemistry of a Single-Layer Graphene Sheet. *Sci. Rep.* **2013**, *3*, 2248.
31. Toth, P. S.; Valota, A. T.; Velicky, M.; Kinloch, I. A.; Novoselov, K. S.; Hill, E. W.; Dryfe, R. A. W. Electrochemistry in a Drop: A Study of the Electrochemical Behaviour of Mechanically Exfoliated Graphene on Photoresist Coated Silicon Substrate. *Chem. Sci.* **2014**, *5*, 582–589.
32. Kobayashi, K. Electronic Structure of a Stepped Graphite Surface. *Phys. Rev. B* **1993**, *48*, 1757–1760.
33. Lai, S. C. S.; Patel, A. N.; McKelvey, K.; Unwin, P. R. Definitive Evidence for Fast Electron Transfer at Pristine Basal Plane

Graphite from High-Resolution Electrochemical Imaging. *Angew. Chem., Int. Ed.* **2012**, *51*, 5405–5408.
34. Patel, A. N.; Collignon, M. G.; O'Connell, M. A.; Hung, W. O. Y.; McKelvey, K.; Macpherson, J. V.; Unwin, P. R. A New View of Electrochemistry at Highly Oriented Pyrolytic Graphite. *J. Am. Chem. Soc.* **2012**, *134*, 20117–20130.
35. Anne, A.; Bahri, M. A.; Chovin, A.; Demaille, C.; Taofifenua, C. Probing the Conformation and 2D-Distribution of Pyrene-Terminated Redox-Labeled Poly(ethylene glycol) Chains End-Adsorbed on HOPG Using Cyclic Voltammetry and Atomic Force Electrochemical Microscopy. *Phys. Chem. Chem. Phys.* **2014**, *16*, 4642–4652.
36. Frederix, P. L. T. M.; Bosshart, P. D.; Akiyama, T.; Chami, M.; Gullo, M. R.; Blackstock, J. J.; Dooleweerdt, K.; de Rooij, N. F.; Staufer, U.; Engel, A. Conductive Supports for Combined AFM–SECM on Biological Membranes. *Nanotechnology* **2008**, *19*, 384004.
37. Lhenry, S.; Leroux, Y. R.; Hapiot, P. Use of Catechol as Selective Redox Mediator in Scanning Electrochemical Microscopy Investigations. *Anal. Chem.* **2012**, *84*, 7518–7524.
38. Kneten, K. R.; McCreery, R. L. Effects of Redox System Structure on Electron-Transfer Kinetics at Ordered Graphite and Glassy Carbon Electrodes. *Anal. Chem.* **1992**, *64*, 2518–2524.
39. Güell, A. G.; Meadows, K. E.; Dudin, P. V.; Ebejer, N.; Macpherson, J. V.; Unwin, P. R. Mapping Nanoscale Electrochemistry of Individual Single-Walled Carbon Nanotubes. *Nano Lett.* **2014**, *14*, 220–224.
40. Güell, A. G.; Meadows, K. E.; Dudin, P. V.; Ebejer, N.; Byers, J. C.; Macpherson, J. V.; Unwin, P. R. Selection, Characterisation and Mapping of Complex Electrochemical Processes at Individual Single-Walled Carbon Nanotubes: The Case of Serotonin Oxidation. *Faraday Discuss.* **2014**, *172*, 439–455.
41. Ebejer, N.; Güell, A. G.; Lai, S. C. S.; McKelvey, K.; Snowden, M. E.; Unwin, P. R. Scanning Electrochemical Cell Microscopy: A Versatile Technique for Nanoscale Electrochemistry and Functional Imaging. *Annu. Rev. Anal. Chem.* **2013**, *6*, 329–351.
42. Blake, P.; Hill, E. W.; Castro Neto, A. H.; Novoselov, K. S.; Jiang, D.; Yang, R.; Booth, T. J.; Geim, A. K. Making Graphene Visible. *Appl. Phys. Lett.* **2007**, *91*, 063124.
43. Güell, A. G.; Ebejer, N.; Snowden, M. E.; Macpherson, J. V.; Unwin, P. R. Structural Correlations in Heterogeneous Electron Transfer at Monolayer and Multilayer Graphene Electrodes. *J. Am. Chem. Soc.* **2012**, *134*, 7258–7261.
44. Ferrari, A. C.; Meyer, J. C.; Scardaci, V.; Casiraghi, C.; Lazzeri, M.; Mauri, F.; Piscanec, S.; Jiang, D.; Novoselov, K. S.; Roth, S.; et al. Raman Spectrum of Graphene and Graphene Layers. *Phys. Rev. Lett.* **2006**, *97*, 187401.
45. Ebejer, N.; Schnippering, M.; Colburn, A. W.; Edwards, M. A.; Unwin, P. R. Localized High Resolution Electrochemistry and Multifunctional Imaging: Scanning Electrochemical Cell Microscopy. *Anal. Chem.* **2010**, *82*, 9141–9145.
46. Valota, A. T.; Kinloch, I. A.; Novoselov, K. S.; Casiraghi, C.; Eckmann, A.; Hill, E. W.; Dryfe, R. A. W. Electrochemical Behavior of Monolayer and Bilayer Graphene. *ACS Nano* **2011**, *5*, 8809–8815.
47. Velický, M.; Bradley, D. F.; Cooper, A. J.; Hill, E. W.; Kinloch, I. A.; Mishchenko, A.; Novoselov, K. S.; Patten, H. V.; Toth, P. S.; Valota, A. T.; et al. Electron Transfer Kinetics on Mono- and Multilayer Graphene. *ACS Nano* **2014**, *8*, 10089–10100.
48. Tan, C.; Rodríguez-López, J.; Parks, J. J.; Ritzert, N. L.; Ralph, D. C.; Abruña, H. D. Reactivity of Monolayer Chemical Vapor Deposited Graphene Imperfections Studied Using Scanning Electrochemical Microscopy. *ACS Nano* **2012**, *6*, 3070–3079.
49. Zhong, J.-H.; Zhang, J.; Jin, X.; Liu, J.-Y.; Li, Q.; Li, M.-H.; Cai, W.; Wu, D.-Y.; Zhan, D.; Ren, B. Quantitative Correlation between Defect Density and Heterogeneous Electron Transfer Rate of Single Layer Graphene. *J. Am. Chem. Soc.* **2014**, *136*, 16609–16617.
50. Patel, A. N.; McKelvey, K.; Unwin, P. R. Nanoscale Electrochemical Patterning Reveals the Active Sites for Catechol Oxidation at Graphite Surfaces. *J. Am. Chem. Soc.* **2012**, *134*, 20246–20249.
51. Zhang, G.; Kirkman, P. M.; Patel, A. N.; Cuharuc, A. S.; McKelvey, K.; Unwin, P. R. Molecular Functionalization of Graphite Surfaces: Basal Plane *versus* Step Edge Electrochemical Activity. *J. Am. Chem. Soc.* **2014**, *136*, 11444–11451.
52. Kirkman, P. M.; Güell, A. G.; Cuharuc, A. S.; Unwin, P. R. Spatial and Temporal Control of the Diazonium Modification of sp^2 Carbon Surfaces. *J. Am. Chem. Soc.* **2014**, *136*, 36–39.
53. Güell, A. G.; Ebejer, N.; Snowden, M. E.; McKelvey, K.; Macpherson, J. V.; Unwin, P. R. Quantitative Nanoscale Visualization of Heterogeneous Electron Transfer Rates in 2D Carbon Nanotube Networks. *Proc. Natl. Acad. Sci. U.S.A.* **2012**, *109*, 11487–11492.
54. Byers, J. C.; Güell, A. G.; Unwin, P. R. Nanoscale Electrocatalysis: Visualizing Oxygen Reduction at Pristine, Kinked, and Oxidized Sites on Individual Carbon Nanotubes. *J. Am. Chem. Soc.* **2014**, *136*, 11252–11255.
55. Martin, J.; Akerman, N.; Ulbricht, G.; Lohmann, T.; Smet, J. H.; von Klitzing, K.; Yacoby, A. Observation of Electron–Hole Puddles in Graphene Using a Scanning Single-Electron Transistor. *Nat. Phys.* **2008**, *4*, 144–148.
56. Wang, Q. H.; Jin, Z.; Kim, K. K.; Hilmer, A. J.; Paulus, G. L. C.; Shih, C.-J.; Ham, M.-H.; Sanchez-Yamagishi, J. D.; Watanabe, K.; Taniguchi, T.; et al. Understanding and Controlling the Substrate Effect on Graphene Electron-Transfer Chemistry *via* Reactivity Imprint Lithography. *Nat. Chem.* **2012**, *4*, 724–732.
57. Rutter, G. M.; Jung, S.; Klimov, N. N.; Newell, D. B.; Zhitenev, N. B.; Stroscio, J. A. Microscopic Polarization in Bilayer Graphene. *Nat. Phys.* **2011**, *7*, 649–655.
58. Partoens, B.; Peeters, F. M. From Graphene to Graphite: Electronic Structure Around the *K* Point. *Phys. Rev. B* **2006**, *74*, 075404.
59. Williams, C. G.; Edwards, M. A.; Colley, A. L.; Macpherson, J. V.; Unwin, P. R. Scanning Micropipet Contact Method for High-Resolution Imaging of Electrode Surface Redox Activity. *Anal. Chem.* **2009**, *81*, 2486–2495.
60. Snowden, M. E.; Güell, A. G.; Lai, S. C. S.; McKelvey, K.; Ebejer, N.; O'Connell, M. A.; Colburn, A. W.; Unwin, P. R. Scanning Electrochemical Cell Microscopy: Theory and Experiment for Quantitative High Resolution Spatially-Resolved Voltammetry and Simultaneous Ion-Conductance Measurements. *Anal. Chem.* **2012**, *84*, 2483–2491.
61. Li, W.; Tan, C.; Lowe, M. A.; Abruña, H. D.; Ralph, D. C. Electrochemistry of Individual Monolayer Graphene Sheets. *ACS Nano* **2011**, *5*, 2264–2270.
62. Ritzert, N. L.; Rodríguez-López, J.; Tan, C.; Abruña, H. D. Kinetics of Interfacial Electron Transfer at Single-Layer Graphene Electrodes in Aqueous and Nonaqueous Solutions. *Langmuir* **2013**, *29*, 1683–1694.
63. Kim, K.; Coh, S.; Kisielowski, C.; Crommie, M. F.; Louie, S. G.; Cohen, M. L.; Zettl, A. Atomically Perfect Torn Graphene Edges and Their Reversible Reconstruction. *Nat. Commun.* **2013**, *4*, 2723.
64. Andrei, E. Y.; Li, G.; Du, X. Electronic Properties of Graphene: A Perspective from Scanning Tunneling Microscopy and Magnetotransport. *Rep. Prog. Phys.* **2012**, *75*, 056501.
65. Li, G.; Luican, A.; Andrei, E. Y. Scanning Tunneling Spectroscopy of Graphene on Graphite. *Phys. Rev. Lett.* **2009**, *102*, 176804.
66. Atamny, F.; Fässler, T. F.; Baiker, A.; Schlögl, R. On the Imaging Mechanism of Monatomic Steps in Graphite. *Appl. Phys. A: Mater. Sci. Process.* **2000**, *71*, 441–447.
67. Pauling, L. The Structure and Properties of Graphite and Boron Nitride. *Proc. Acad. Natl. Sci. U.S.A.* **1966**, *56*, 1646.
68. Li, Z.; Wang, Y.; Kozbial, A.; Shenoy, G.; Zhou, F.; McGinley, R.; Ireland, P.; Morganstein, B.; Kunkel, A.; Surwade, S. P.; et al. Effect of Airborne Contaminants on the Wettability of Supported Graphene and Graphite. *Nat. Mater.* **2013**, *12*, 925–931.

69. Macpherson, J. V.; Unwin, P. R. Combined Scanning Electrochemical−Atomic Force Microscopy. *Anal. Chem.* **2000**, *72*, 276–285.
70. Kranz, C.; Friedbacher, G.; Mizaikoff, B. Integrating an Ultramicroelectrode in an AFM Cantilever: Combined Technology for Enhanced Information. *Anal. Chem.* **2001**, *73*, 2491–2500.
71. Patel, A. N.; Tan, S.-y.; Miller, T. S.; Macpherson, J. V.; Unwin, P. R. Comparison and Reappraisal of Carbon Electrodes for the Voltammetric Detection of Dopamine. *Anal. Chem.* **2013**, *85*, 11755–11764.
72. Patel, A. N.; Tan, S.-y.; Unwin, P. R. Epinephrine Electrooxidation Highlights Fast Electrochemistry at the Graphite Basal Surface. *Chem. Commun.* **2013**, *49*, 8776–8778.
73. McCreery, R. L.; Bergren, A.; Morteza-Najarian, A.; Sayed, S. Y.; Yan, H. Electron Transport in All-Carbon Molecular Electronic Devices. *Faraday Discuss.* **2014**, *172*, 9–25.
74. Chang, H.; Bard, A. J. Observation and Characterization by Scanning Tunneling Microscopy of Structures Generated by Cleaving Highly Oriented Pyrolytic Graphite. *Langmuir* **1991**, *7*, 1143–1153.
75. McDermott, M. T.; McCreery, R. L. Scanning Tunneling Microscopy of Ordered Graphite and Glassy Carbon Surfaces: Electronic Control of Quinone Adsorption. *Langmuir* **1994**, *10*, 4307–4314.
76. Stevens, F.; Kolodny, L. A.; Beebe, T. P. Kinetics of Graphite Oxidation: Monolayer and Multilayer Etch Pits in HOPG Studied by STM. *J. Phys. Chem. B* **1998**, *102*, 10799–10804.
77. Zoval, J. V.; Stiger, R. M.; Biernacki, P. R.; Penner, R. M. Electrochemical Deposition of Silver Nanocrystallites on the Atomically Smooth Graphite Basal Plane. *J. Phys. Chem.* **1996**, *100*, 837–844.
78. Ma, H.; Lee, L.; Brooksby, P. A.; Brown, S. A.; Fraser, S. J.; Gordon, K. C.; Leroux, Y. R.; Hapiot, P.; Downard, A. J. Scanning Tunneling and Atomic Force Microscopy Evidence for Covalent and Noncovalent Interactions between Aryl Films and Highly Ordered Pyrolytic Graphite. *J. Phys. Chem. C* **2014**, *118*, 5820–5826.
79. McCreery, R. L. Advanced Carbon Electrode Materials for Molecular Electrochemistry. *Chem. Rev.* **2008**, *108*, 2646–2687.
80. Spanu, L.; Sorella, S.; Galli, G. Nature and Strength of Interlayer Binding in Graphite. *Phys. Rev. Lett.* **2009**, *103*, 196401.
81. Li, G.; Luican, A.; Lopes dos Santos, J. M. B.; Castro Neto, A. H.; Reina, A.; Kong, J.; Andrei, E. Y. Observation of Van Hove Singularities in Twisted Graphene Layers. *Nat. Phys.* **2010**, *6*, 109–113.
82. Chen, S.; Liu, Y.; Chen, J. Heterogeneous Electron Transfer at Nanoscopic Electrodes: Importance of Electronic Structures and Electric Double Layers. *Chem. Soc. Rev.* **2014**, *43*, 5372–5386.
83. Castro Neto, A. H.; Guinea, F.; Peres, N. M. R.; Novoselov, K. S.; Geim, A. K. The Electronic Properties of Graphene. *Rev. Mod. Phys.* **2009**, *81*, 109–162.
84. Kobayashi, Y.; Fukui, K.; Enoki, T. Edge State on Hydrogen-Terminated Graphite Edges Investigated by Scanning Tunneling Microscopy. *Phys. Rev. B* **2006**, *73*, 125415.
85. Gerischer, H.; McIntyre, R.; Scherson, D.; Storck, W. Density of the Electronic States of Graphite: Derivation from Differential Capacitance Measurements. *J. Phys. Chem.* **1987**, *91*, 1930–1935.
86. Luque, N. B.; Schmickler, W. Are the Reactions of Quinones on Graphite Adiabatic? *Electrochim. Acta* **2013**, *88*, 892–894.
87. Bard, A. J.; Faulkner, L. R. *Electrochemical Methods: Fundamentals and Applications*, 2nd ed.; John Wiley & Sons, Inc.: New York, 2001; pp 115−132.
88. Cline, K. K.; McDermott, M. T.; McCreery, R. L. Anomalously Slow Electron Transfer at Ordered Graphite Electrodes: Influence of Electronic Factors and Reactive Sites. *J. Phys. Chem.* **1994**, *98*, 5314–5319.
89. Sato, N. *Electrochemistry at Metal and Semiconductor Electrodes*, 2nd ed.; Elsevier Science: Amsterdam, 2003; pp 213−248.
90. Heller, I.; Kong, J.; Williams, K. A.; Dekker, C.; Lemay, S. G. Electrochemistry at Single-Walled Carbon Nanotubes: The Role of Band Structure and Quantum Capacitance. *J. Am. Chem. Soc.* **2006**, *128*, 7353–7359.
91. Heller, I.; Kong, J.; Heering, H. A.; Williams, K. A.; Lemay, S. G.; Dekker, C. Individual Single-Walled Carbon Nanotubes as Nanoelectrodes for Electrochemistry. *Nano Lett.* **2005**, *5*, 137–142.
92. Xia, J.; Chen, F.; Li, J.; Tao, N. Measurement of Quantum Capacitance of Graphene. *Nat. Nanotechnol.* **2009**, *4*, 505–509.